SCIENCE CHINA
Earth Sciences

•RESEARCH PAPER•

July 2021 Vol.64 No.7: 1184–1194
https://doi.org/10.1007/s11430-020-9790-1

A H_2O-in-zircon perspective on the heterogeneous water content of crust-derived magmas in southern Tibet

Juntong MENG[1,2,3], Xiaoping XIA[1,2*], Lin MA[1,2], Ziqi JIANG[4], Jian XU[1,2,3], Zexian CUI[1,2], Qing YANG[1,2], Wanfeng ZHANG[1,2] & Le ZHANG[1,2]

[1] *State Key Laboratory of Isotope Geochemistry, Guangzhou Institute of Geochemistry, Chinese Academy of Sciences, Guangzhou 510640, China;*
[2] *CAS Center for Excellence in Deep Earth Science, Guangzhou 510640, China;*
[3] *College of Earth and Planetary Science, University of Chinese Academy of Sciences, Beijing 100049, China;*
[4] *School of Earth Science, Guilin University of Technology, Guilin 541004, China*

Received December 25, 2020; revised April 30, 2021; accepted May 11, 2021; published online June 11, 2021

Abstract Geophysical and geochemical evidence revealed that certain amounts of water are stored in the Earth's interior, and its distribution exhibits temporal and spatial differences. Recent studies indicate that the H_2O-in-zircon has a potential to reveal magma water content. Using secondary ion mass spectrometry (SIMS), we analyzed the zircon water content and oxygen isotopes in granitoids (two-mica granite, quartz monzonite, diorite, and granodiorite) from southern Tibet. The results are used to explore the diversity of water content in crust-derived magmas, which is also supported by the LA-ICPMS zircon trace element analysis. There are low zircon water contents for two partial melting products of the ancient crust (peak at 85 and 300 ppm, respectively). Meanwhile, there are high H_2O-in-zircon peaks (435 and 475 ppm, respectively) for two partial melting products of the juvenile crust. The calculated radiation damage accumulation in these zircon grains is below 3×10^{15} α decay events mg^{-1}, suggesting that the zircon grains are well crystalline. There is no correlation between REE+Y and H+P, indicating that the mechanism of charge balance for water uptaking into zircon, in which the excess of REE+Y to P controls H content, is not applicable to the studied samples. The degree of magma fractionation cannot account for the zircon water content variation, because there is no co-variation between zircon Hf and H_2O contents. Similarly, the degree of partial melting was unlikely to be responsible for the H_2O-in-zircon distinction. We interpret that the H_2O-in-zircon variation reflects the influence of melting mode (dehydration vs. water-fluxed) and water content in the crustal source. In the Late Devonian, dehydration melting of the crustal rocks was facilitated at elevated temperatures, which produced magmas with the lowest water contents. Water-fluxed melting of the ancient crust would produce relatively "drier" magma than water-fluxed melting of the juvenile crust.

Keywords H_2O-in-zircon, SIMS, dehydration melting, water-fluxed melting, magma water content

Citation: Meng J, Xia X, Ma L, Jiang Z, Xu J, Cui Z, Yang Q, Zhang W, Zhang L. 2021. A H_2O-in-zircon perspective on the heterogeneous water content of crust-derived magmas in southern Tibet. Science China Earth Sciences, 64(7): 1184–1194, https://doi.org/10.1007/s11430-020-9790-1

1. Introduction

Nominally anhydrous minerals (NAMs) contain trace amounts of water in the form of molecular hydrogen, ammonium, hydroxyl, or H_2O molecules (Johnson, 2006; Watenphul et al., 2010; Yang X et al., 2016), constituting an important water reservoir in the Earth's interior (Bell and Rossman, 1992). Minute water content change in NAMs has significant effects on the rock physicochemical properties, such as the electrical conductivity (Karato, 1990; Yang et al.,

* Corresponding author (email: xpxia@gig.ac.cn)

2006) and melting point (Seaman et al., 2013). As revealed by many geophysical studies, the continental crust is characterized by heterogeneous electrical conductivity: High conductivity in subduction zones and low conductivity in cratons (Hyndman and Shearer, 1989; Bai et al., 2010; Worzewski et al., 2010; Evans et al., 2014; Manning, 2018). This phenomenon may be related to the heterogeneous distribution of water content in the crust. Water content variation of NAMs from some lower crustal granulites also suggests that the water content in the lower crust is heterogeneous (Yang et al., 2008; Yang et al., 2012a, 2012b; Németh et al., 2015; Schmädicke et al., 2015; Zhang L et al., 2018). However, few studies were conducted on elucidating the water content difference between the magmas generated in different sources.

As a common accessory mineral in felsic rocks, zircon is physically and chemically inert and has a very high U-Pb closure temperature (up to 900°C) (Cherniak and Watson, 2001). Compared with other NAMs, hydrogen diffusion in zircon is slower with higher activation energy, and thus the initial water content information is more likely to be retained (Zhang, 2015). Previously, much research attention has been paid on zircon U-Pb dating, trace element and O-Hf-Li isotope analyses (Belousova et al., 2002; Valley, 2003; Xia et al., 2006; Trail et al., 2007; Ushikubo et al., 2008; Trail et al., 2018), whereas research on H_2O in zircon was largely inadequate due to the limited analytical technology and the uncertainties in the water uptake mechanism in zircon (De Hoog et al., 2014; Xia et al., 2019). In this study, we analyzed the H_2O contents and trace element and oxygen isotope compositions of the zircon grains from granitoids (with different crustal sources) in southern Tibet. Our results indicated that the zircon H_2O content difference in magmatic rocks of different crustal sources can reflect the variation of H_2O content in the magmas. Subsequently, we discussed the possible reasons for the H_2O content variations in these magmas.

2. Geological background and sample descriptions

Our four rock samples were collected from the southern margin of the Lhasa block, and consist of a Late Devonian Zhengga two-mica granite, an Oligocene Chongmuda quartz monzonite, a Late Cretaceous diorite and an Eocene granodiorite from the Chanang-Zedang area.

The Lhasa block is bounded by the Bangong-Nujiang and Yarlung-Tsangpo suture in the north and south, respectively (Yin and Harrison, 2000; Zhu et al., 2013). The Gangdese batholith in the southern Lhasa block contains mainly diorite, granodiorite, monzonite, and granite, with sparse occurrences of ultramafic-mafic rocks (e.g., gabbro). According to published geochronological data, four magmatic phases are present in the batholith at 205–102, 109–80, 65–41, and 33–13 Ma (Ji et al., 2009). Positive zircon $\varepsilon_{Hf}(t)$ values are commonly found in the rocks from the batholith, indicating a juvenile magma source. Late Devonian igneous rocks with negative zircon $\varepsilon_{Hf}(t)$ values were identified in recent years, and have been interpreted as partial melting products of the ancient crust (Ji et al., 2012).

2.1 Late Devonian Zhengga two-mica granite

The Zhengga two-mica granite was formed at ~360 Ma and intruded by Cretaceous gabbro and Paleocene granite. Its gneissic structure was possibly formed during the ca. 105–102 Ma amphibolite-facies metamorphism (Dong et al., 2014). Detailed petrological and geochemical studies were conducted by Ma et al. (2019). The two-mica granite has mainly quartz (30–40 vol.%), K-feldspar (30–35 vol.%), plagioclase (5–10 vol.%), biotite (10–15 vol.%), and muscovite (5–8 vol.%), with accessory (<5 vol.%) garnet and Fe-Ti oxides. The sample 11SR02-1 has SiO_2=73.71 wt.%, MgO=0.84 wt.%, A/CNK=1.18, $Mg^{\#}$=47.5, K_2O/Na_2O=0.69, Sr/Y=3.9, Zr/Hf=32.02, and $\varepsilon_{Nd}(t)$=–8.61. The sample is zircon U-Pb dated to be 364.6±2.5 Ma. The zircons display negative $\varepsilon_{Hf}(t)$ and high $\delta^{18}O$ values, suggesting ancient source or sediment addition (Ma et al., 2019). The associated bimodal metamorphic rocks have back-arc basin basalt (BABB) affinity, implying that the Devonian Zhengga granite was formed in a back-arc extensional setting (Dong et al., 2014; Ma et al., 2019).

2.2 Oligocene Chongmuda quartz monzonite

The Chongmuda granitoids are located 10–15 km west of Sangri County, and include quartz monzonite with minor granodiorite. Detailed information on these rocks was introduced by Jiang et al. (2011). The quartz monzonite consists mainly of plagioclase (45–48 vol.%), K-feldspar (30–34 vol.%), quartz (10–14 vol.%), amphibole (5–8 vol.%), biotite (3–5 vol.%), and minor accessory minerals. The quartz monzonite sample 07TB11 has SiO_2=64.70 wt.%, MgO=2.24 wt.%, A/CNK=0.93, $Mg^{\#}$=51, K_2O/Na_2O=1.05, Sr/Y=89.3, Zr/Hf=34.9, $\varepsilon_{Nd}(t)$=–3.15. The sample is zircon U-Pb dated to be 30.2±0.7 Ma, with zircon $\varepsilon_{Hf}(t)$=4.2±0.5. Compared with other late Mesozoic igneous rocks in the Gangdese belt, sample 07TB11 has higher whole-rock $(^{87}Sr/^{86}Sr)_i$ and $\varepsilon_{Nd}(t)$ values, and falls into the fourth quadrant in the $(^{87}Sr/^{86}Sr)_i$ vs. $\varepsilon_{Nd}(t)$ plot, similar to many adakitic rocks (ca. 26–10 Ma) in the Gangdese belt. The Chongmuda quartz monzonitic magma was likely sourced from the lower crust of the Indian plate, possibly contaminated by the depleted mantle during the magma ascent (Jiang et al., 2011).

2.3 Late Cretaceous diorite and Eocene granodiorite in Chanang-Zedang area

From the Jurassic to the Tertiary, extensive magma emplacement had likely occurred in the Chanang-Zedang area (Jiang et al., 2014). A ~75 Ma diorite body at the Luomu village (ca. 10 km east of Shannan city) was reported (Jiang et al., 2014), which contains mainly plagioclase (35–40 vol.%), amphibole (25–30 vol.%), K-feldspar (10–15 vol.%), quartz (5–10 vol.%), mica (5–10 vol.%), and minor accessory minerals. A ~48 Ma granodiorite was identified in the Lamda village, and is composed of plagioclase (30–35 vol.%), amphibole (20–25 vol.%), K-feldspar (10–15 vol.%), biotite (10–15 vol.%), quartz (5–10 vol.%), and accessory minerals (Jiang et al., 2014). For the whole-rock geochemical results, the diorite sample 07TB18 has SiO_2=60.24 wt.%, MgO=2.96 wt.%, $Mg^{\#}$=48, A/CNK=0.90, K_2O/Na_2O=0.69, Sr/Y=24.4, Zr/Hf=32.0, $(^{87}Sr/^{86}Sr)_i$=0.704515, and $\varepsilon_{Nd}(t)$=3.04. The sample was zircon U-Pb dated to be 47.9±0.1 Ma and has zircon $\varepsilon_{Hf}(t)$=10.9±0.4. The granodiorite sample 07TB18 has SiO_2=65.86 wt.%, MgO=1.66 wt.%, $Mg^{\#}$=42, A/CNK=0.97, K_2O/Na_2O=1.06, Sr/Y=16.2, Zr/Hf=36.8, $(^{87}Sr/^{86}Sr)_i$ =0.704503, and $\varepsilon_{Nd}(t)$=3.01. The sample is zircon U-Pb dated to be 47.9±0.1 Ma, and has zircon $\varepsilon_{Hf}(t)$=10.9±0.4. Both samples 07TB18 and 09TB128 have low MgO-Cr-Ni contents and $Mg^{\#}$, and have depleted Sr-Nd-Hf isotope compositions. This indicates that both samples may have had a juvenile lower crustal magma source (Jiang et al., 2014).

3. Analytical methods

Zircon grains were separated from the crushed rock samples by conventional heavy liquid and magnetic techniques. The separated zircon grains were casted on a double adhesive tape. A hollow cylinder was placed above the double adhesive tape and Sn alloy (52% Sn+48% Bi) molten at 110°C was poured into a hollow cylinder. The sample was placed inside a vacuum chamber at 110°C for at least 30 minutes to expel any gas from the mounts. When temperature of the vacuum chamber falls back to room temperature, the mounts were removed for washing and polishing. Detailed sample preparation procedures were similar to those described by Zhang W et al. (2018).

Zircon water content and oxygen isotopes were measured simultaneously with a CAMECA IMS 1280-HR secondary ion mass (SIMS) spectrometer installed at the State Key Laboratory of Isotope Geochemistry, Guangzhou Institution of Geochemistry, Chinese Academy of Sciences (GIGCAS). A 3–5 nA Cs^+ primary beam was accelerated at 10 kV, and the secondary ion beam was extracted with −10 kV energy. A normal-incidence electron gun was used to compensate the charge near the analysis spot. The ^{16}O and ^{18}O signals were collected by two Faraday cup detectors, and $^{16}O^1H$ signals were collected by an electron multiplier. Collector slits of 500 μm was used for both ^{16}O and ^{18}O signal, with a mass resolving power of ~2500. Collector slit of ~173 nm was used for $^{16}O^1H$ signal, with a mass resolving power of ~7000 to avoid the interference by ^{17}O. A nuclear magnetic resonance (NMR) controller was used to lock the magnetic field. Single analytical run contains ~200 s pre-sputtering and beam alignment (centering DTFA and DTCA), and 60 s for data acquisition (16 integrated cycles). Calibrated curve was established based on analytical $^{16}O^1H/^{16}O$ ratios and FTIR (Fourier Transform Infrared Spectroscopy) H_2O contents of standard materials (Xia et al., 2019). The H_2O-in-zircon of samples was calculated based on the fitting equation. The measured $^{18}O/^{16}O$ ratios are normalized to the Vienna Standard Mean Ocean Water compositions (SMOW) notated as $\delta^{18}O_M$. Instrument mass fractionation (IMF) was calculated according to the Penglai zircon $\delta^{18}O$ value (Li et al., 2010), and the data obtained were deduced with the equation of $\delta^{18}O=\delta^{18}O_M$–IMF.

Zircon trace element concentrations were measured with an ELEMENT XR inductively coupled plasma-sector field-mass spectrometry (ICP-SF-MS), equipped with a Resonetic RESOlution M-50 193 nm ArF excimer laser ablation system. The analysis sites overlapped with the SIMS spots. The laser repetition rate was 5 Hz, with ~4 J cm^{-2} energy density impacted on a 33 μm diameter spot. Analysis time of a single spot was 50 s, including 20 s laser-off background acquisition and 30 s laser-on sample data acquisition. Helium was used as the carrier gas for the aerosol transport into the mass spectrometer. The nuclides detected include: ^{25}Mg, ^{27}Al, ^{29}Si, ^{31}P, ^{49}Ti, ^{57}Fe, ^{89}Y, ^{139}La, ^{140}Ce, ^{141}Pr, ^{145}Nd, ^{149}Sm, ^{151}Eu, ^{155}Gd, ^{159}Tb, ^{163}Dy, ^{165}Ho, ^{167}Er, ^{169}Tm, ^{172}Yb, ^{175}Lu, ^{178}Hf. Reference material NIST SRM 610 was used as the external standard for mass bias and instrument drift calibration. ^{29}Si concentration was used as the internal standard, and NIST SRM 612 was used to monitor the analytical reliability. Analyses of NIST 612 yielded analytical error and precision within 10%. Detailed analytical processes and data reduction strategy were the same as those introduced by Zhang et al. (2019).

4. Results

4.1 Zircon CL image

Typical zircon cathodoluminescence (CL) images were shown in Figure 1. Nearly all zircon grains are euhedral-subhedral prismatic with aspect ratios of 3:2 to 3:1. Zircon grains from sample 11SR02-1 (100–200 μm long, 60–100 μm wide) are slightly smaller than those from the other samples, and are characterized by the presence of oscillatory zoning and core-rim texture. Several zircon grains

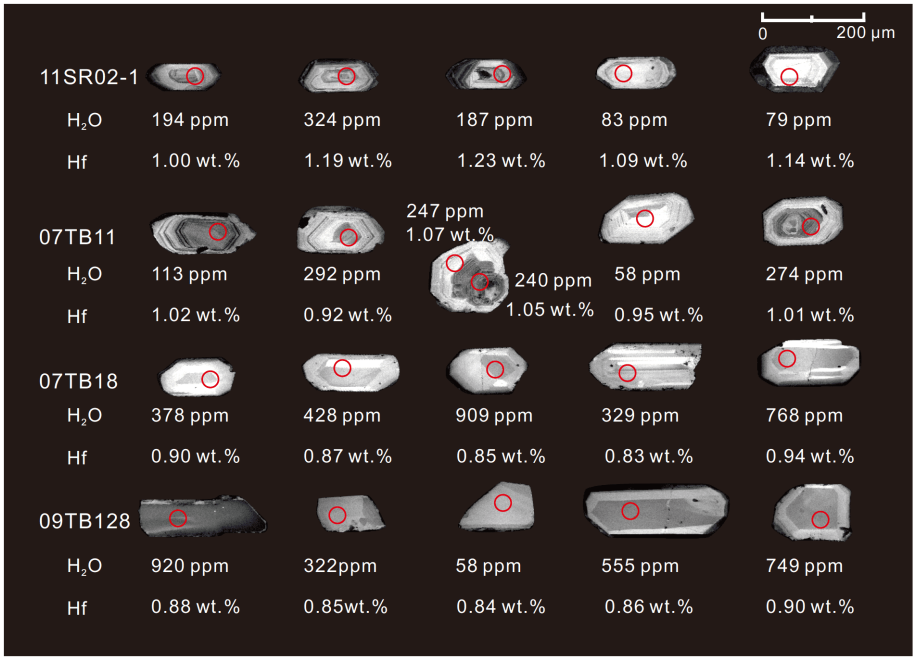

Figure 1 Representative zircon CL images. Circles denote analysis spots of SIMS and LA-ICPMS.

from samples 07TB11, 07TB18, and 09TB128 have their lengths up to 300 μm. Apart from oscillatory zoning, zircon grains from sample 07TB11 have dark cores and bright rims in CL images, whereas oscillatory zoning is absent in the zircons from samples 07TB18 and 09TB128. Different zircon CL reflectance is present for the samples 07TB18 and 09TB128, similar to many zircon grains from mafic rocks (Corfu et al., 2003). Zones of different CL reflectance of samples 11SR02-1 and 07TB11 have nearly identical U-Pb ages (Jiang et al., 2011; Ma et al., 2019).

4.2 Zircon water content and $\delta^{18}O$ value

Results of zircon water contents and $\delta^{18}O$ values are listed in Appendix Table S1 (http://link.springer.com). Several analysis data are discarded due to their large $^{16}O^{1}H/^{16}O$ uncertainties and/or extremely high contents of Mg, Fe, and Al, which may be caused by impurities in the cracks on zircon grains (Geisler et al., 2002; Pidgeon et al., 2019). The two-mica granite sample 11SR02-1 (~360 Ma) has a wide H_2O-in-zircon range (60–838 ppm, average=251 ppm, median=174 ppm), and one prominent peak (85 ppm) in the kernel density plot (Figure 2a). The quartz monzonite sample 07TB11 (~30 Ma) has a slightly narrower water-in-zircon range (58–578 ppm, average=251 ppm, median=256 ppm), with two main H_2O peaks at 190 ppm and 300 ppm (Figure 2b). The diorite 07TB18 (~75 Ma) and granodiorite 09TB128 (~48 Ma) have higher water-in-zircon contents: 07TB18: 179–909 ppm (average=448 ppm, median=434 ppm); 09TB128: 58–920 ppm (average=416 ppm, median=445 ppm). In the kernel density plot, the H_2O-in-zircon peaks of samples 07TB18 and 09TB128 are 435 ppm and 475 ppm (Figure 2c and 2d), respectively, yielding a H_2O-in-zircon relation of 11SR02-1<07TB11<07TB18≈09TB128 (Figures 2 and 3). Oxygen isotope compositions of 11SR02-1 (6.00–11.34‰, average=8.86‰) are similar to the $\delta^{18}O$ results reported by Ma et al. (2019). Average $\delta^{18}O$ values of the other zircon grains from samples 07TB11 (5.72‰), 07TB18 (6.12‰), and 09TB128 (6.07‰) are considerably lower (Figure 4).

4.3 Trace element contents

Trace elements concentrations of the zircon samples are listed in Appendix Table S2. The samples have Hf contents of 8540–13300 ppm (11SR02-1), 7970–11500 ppm (07TB11), 7850–11100 ppm (07TB18), and 7090–9080 ppm (09TB128), with their average Hf contents in the order of 07TB18≈09TB128<07TB11<11SR02-1. Within each sample, there is no correlation between Hf and H_2O contents (Figure 5). The atomic contents of (H+P) are higher than (REE+Y), and no correlation is present between them (Figure 6).

5. Discussion

5.1 Controlling factors of H_2O content in zircon

5.1.1 Radiation damage to the studied zircons

In zircon, Zr^{4+} is commonly substituted by radioactive elements of U and Th (Hoskin and Schaltegger, 2003). The radioactive particles emitted by U-Th decay are responsible

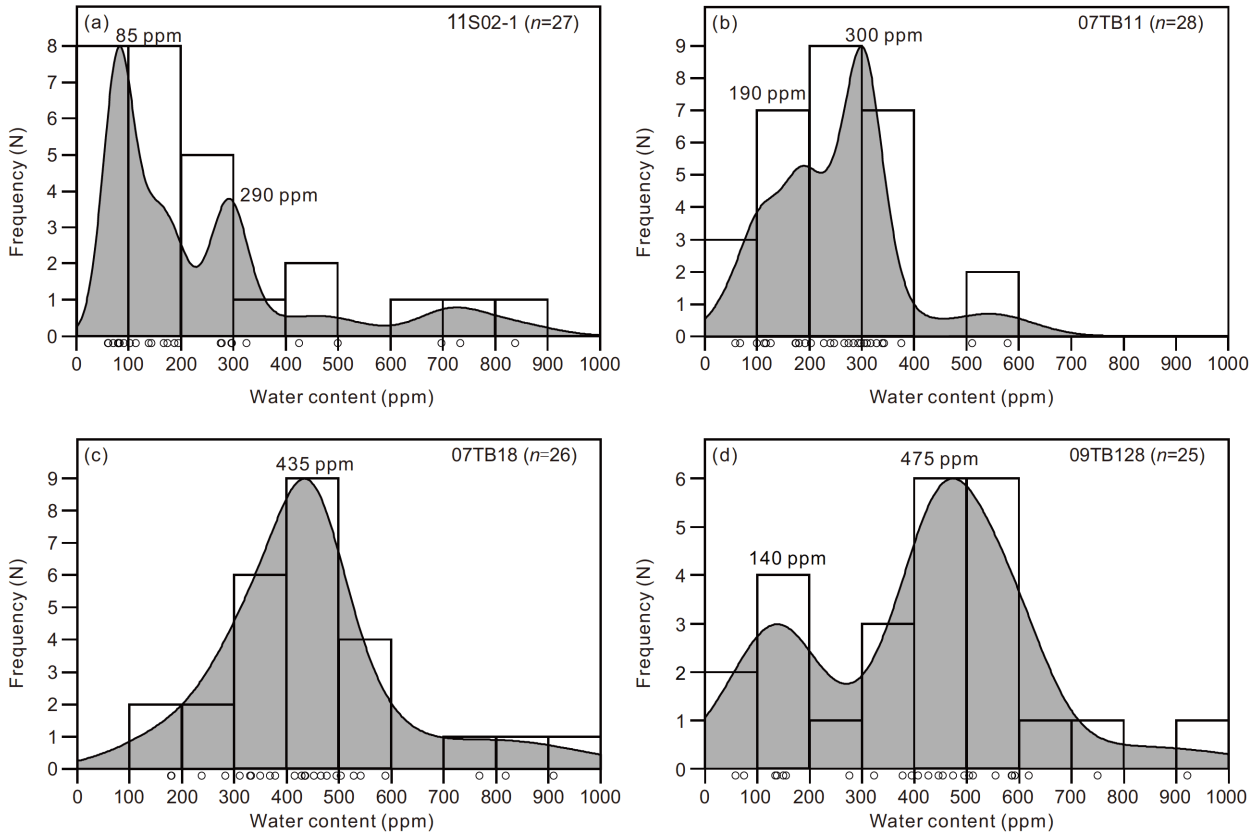

Figure 2 Kernel density plots of H_2O-in-zircon: (a) 11SR02-1; (b) 07TB11; (c) 07TB18; (d) 09TB128.

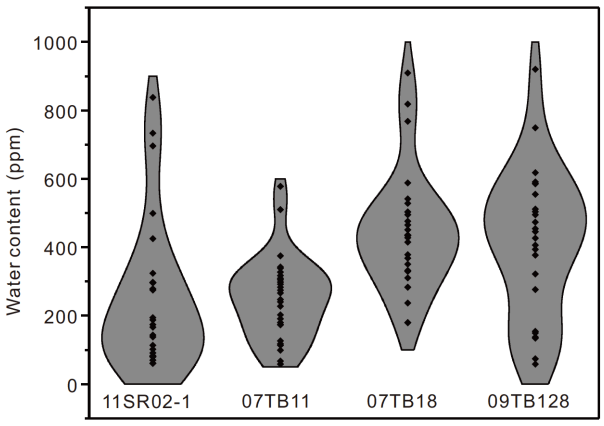

Figure 3 Violin plot of H_2O-in-zircon.

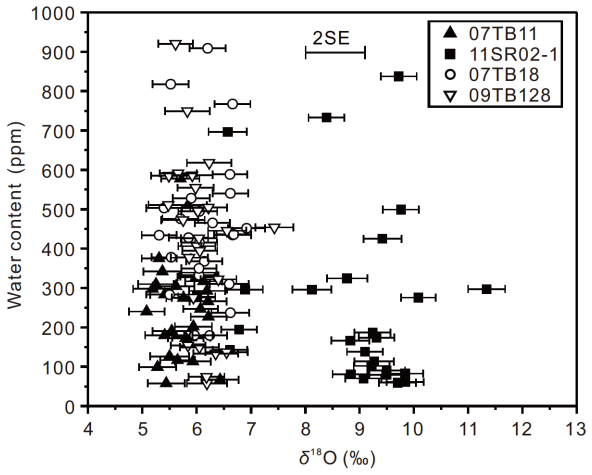

Figure 4 H_2O vs. $\delta^{18}O$ plot of zircons.

for the formation of metamict zircons. Compared with non-metamict zircons, metamict zircons have distinct unit-cell parameter, density, and refractive index (Chakoumakos et al., 1987). It is noteworthy that metamict zircons contain abundant Ca, Fe, Al and H_2O, probably due to metasomatism (Geisler et al., 2002; Pidgeon et al., 2019). In the Sri Lanka gem-quality zircons, hydroxyl (OH) absorption band was not detected in the samples with α-decay dose<4.5×10^{15} events mg^{-1}, which indicates that water in these metamict zircons has a secondary origin (Woodhead et al., 1991). The radiation damage accumulation in zircons can be calculated with the equation of $D=8N_1[\exp(\lambda_1 t)-1]+7N_2[\exp(\lambda_2 t)-1]+6N_3[\exp\lambda_3 t)-1]$ (Murakami et al., 1991), where D=α-decay dose (events mg^{-1}); N_1, N_2, N_3=number (atoms mg^{-1}) of ^{238}U, ^{235}U, and ^{232}Th, respectively; λ_1, λ_2, λ_3=decay constant (yr^{-1}) of ^{238}U, ^{235}U, and ^{232}Th, respectively; t=zircon crystallization age (yr). When D is less than 3×10^{15} events mg^{-1}, zircons

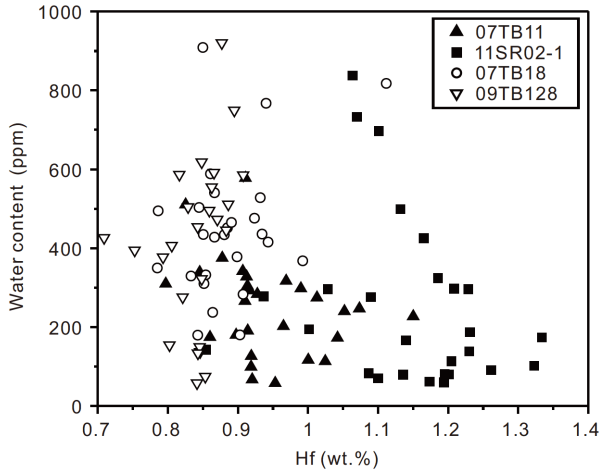

Figure 5 H_2O vs. Hf plot of zircons.

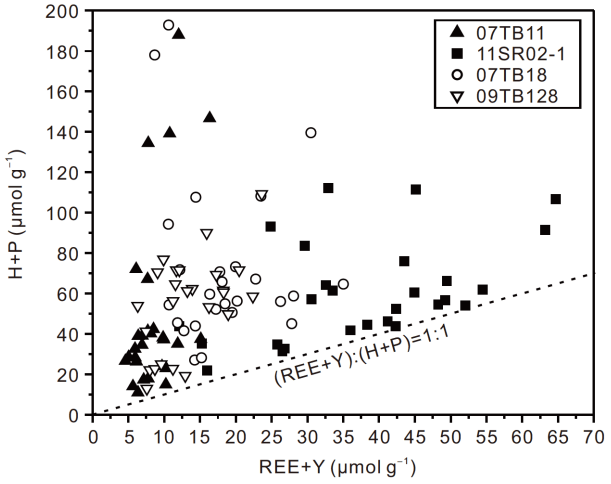

Figure 6 (H+P) vs. (REE+Y) plot. Dash line denotes 1:1 (REE+Y)/(H+P) ratio.

with minor damage accumulation display point defects (Murakami et al., 1991). We calculated the sample α-decay dose according to the published U-Pb geochronological data (Jiang et al., 2011, 2014; Ma et al., 2019), and the results indicate weak radiation damage (α-decay dose<3×10^{15} events mg^{-1}). Zircon analyses with extremely-high Mg, Fe, and Al contents are discarded due to the possible influence by zircon-fluid interactions. In addition, low $\delta^{18}O$ values and negative correlations between $\delta^{18}O$ and H_2O-in-zircon are prevalent in altered zircons (Pidgeon et al., 2013; Wang et al., 2014; Pidgeon et al., 2017), yet these features are not found in our four samples (Figure 4). This suggests that the water incorporated into our zircon samples is predominantly primary.

5.1.2 Zircon crystallization temperature, pressure, and oxygen fugacity

The H_2O partition coefficient (D_{H2O}) between zircon and its melt is still unknown, whilst that of other NAMs correlates negatively with temperature but positively with pressure (Demouchy and Bolfan-Casanova, 2016). However, the trace element partition coefficients between zircon and its melt show identical trends with temperature and pressure, similar to those of other NAMs (Rubatto and Hermann, 2007). In this study, therefore, we assume that the zircon D_{H2O} has similar correlations with the temperature and pressure. The temperatures calculated with the Ti-in-zircon thermometer and the pressures calculated from Sr/Y ratios of the rock samples (Jiang et al., 2014; Ma et al., 2019) are listed in Table 1. The Chongmuda quartz monzonite sample 07TB11 (sourced from the ancient lower crust of the Indian plate) is characterized by low temperature and high pressure, and its zircons possess high D_{H2O}. The zircon H_2O content of sample 07TB11 is markedly lower than that of samples 07TB18 and 09TB128 (sourced from the juvenile crust in the Gangdese belt). Comparatively, pressure likely exerts smaller influence on zircon D_{H2O} than temperature (Rubatto and Hermann, 2007; Luo and Ayers, 2009). Because sample 11SR02-1 has lower temperature and pressure than sample 09TB128, the zircon D_{H2O} of sample 11SR02-1 is equal to (or slightly higher than) that of sample 09TB128. However, the H_2O-in-zircon content of sample 11SR02-1 is clearly lower than that of sample 09TB128. Therefore, temperature and pressure are unlikely to be the key controlling factors of H_2O contents in zircons.

Zircon Ce and Eu anomalies can reflect the magma oxygen fugacity (fO_2), with higher Ce/Ce^* and Eu/Eu^* signifying

Table 1 Estimated whole-rock temperature, pressure and oxygen fugacity conditions of the samples in this study[a)]

	11SR02-1	07TB11	07TB18	09TB128
Average Ti-in-zircon temperature (°C)	784	704	782	828
Whole-rock Sr/Y ratio	3.9	89.3	24.4	16.2
Melting depth (km)	12	107	35	26
Pressure (GPa)	0.37	3.22	1.06	0.78
Average zircon Ce/Ce^*	8.6	95.8	49.2	66.1

a) The Sr-Y contents are from Jiang et al. (2014) and Ma et al. (2019). Calculation method of the Ti-in-zircon thermometry follows that of Ferry and Watson (2007), assuming the activities of SiO_2=1.00 and TiO_2=0.75. The calculated melting depths are based on Chapman et al. (2015), with the pressure gradient=0.03 GPa km^{-1} (Hu et al., 2003).

higher fO_2 (Burnham and Berry, 2012). Our results indicate that there is no correlation between zircon Ce/Ce^* and H_2O contents (Table 1). Considering that no relations between invariant elements and fO_2 were observed (Burnham and Berry, 2012), we deduce that fO_2 has little influence on the H_2O-in-zircon content.

It is noteworthy that each of our samples has wide H_2O-in-zircon range. Data from the inherited zircons are discarded because of possible inherited cores (based on CL images). To assess the degree of H-diffusion in zircons, we calculated the H-diffusion time in zircons at different grain sizes and temperatures, based on the diffusion law at [001] (perpendicular to the *a* axis) (Zhang, 2015) (Figure 7). Assuming that our igneous rock samples were emplaced at ca. 12–23 km (middle crust) and geothermal gradient is 15°C km^{-1} (Sun et al., 2018), the temperature range is calculated to be ca. 180–345°C. In this temperature range, the duration for total H diffusion is much longer than 100 million years (Myr) (Figure 7), and thus the H signature was likely retained after the temperatures drop back to ca. 180–345°C. There is no evidence to support late high-temperature metamorphism in our rock samples, and hence the possibility of late diffusion and re-equilibrium is very low. Furthermore, there is no correlation between the zircon size and H_2O contents in our samples, and there is no H_2O-in-zircon decrease from the zircon core to zircon rim (sample 07TB11) (Figure 1). In summary, the water incorporated into the studied zircons can reflect the water incorporation when these zircons were crystallized, whilst the water content variation within individual sample may be attributed to the fluctuated magma water content and temperature during the zircon crystallization.

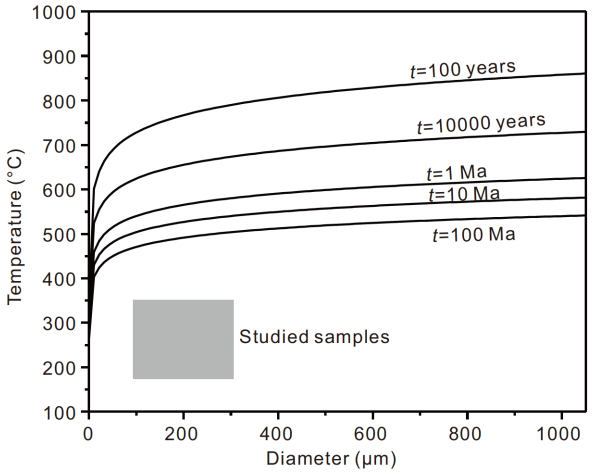

Figure 7 Zircon H diffusion time diagram with different grain sizes and temperatures. Gray field represents the data range of the analyzed zircon in this study.

5.1.3 *Timing of zircon crystallization in the magma evolution*

Water is incompatible and its content would increase with magma fractionation (e.g., Wu et al., 2017). Only the water contents of early-crystallized zircons can record the initial H_2O content of the magma. Zircons generally crystallize early in the less-evolved I-type and S-type granites, but they crystallize throughout the magma fractionation in alkaline granites and highly-fractionated granites (Collins et al., 1982; Breiter et al., 2014). Our four samples fall inside the sub-alkaline field in the SiO_2 vs. (Na_2O+K_2O) plot (Jiang et al., 2014; Ma et al., 2019), and are thus not alkali granites. In addition, all these samples have low 1000*Ga/Al ratios and fall inside the normal I-/S-type granite field (Zr/Hf=32–37). Moreover, the samples have flat chondrite-normalized REE patterns (Jiang et al., 2014; Ma et al., 2019), and are thus not highly-fractionated granites (Whalen et al., 1987; Bau, 1996; Wu et al., 2017). This implies that our zircon samples were crystallized in the early magma fractionation stage.

5.1.4 *Degree of partial melting*

Similar to H_2O, Hf is incompatible in the magmas (Sun and McDonough, 1989; Hauri et al., 2006). Degree of partial melting is negatively correlated with the magma Hf and H_2O contents. Since our zircon samples likely crystallized early in the magma evolution, the zircon Hf content was used to constrain the degree of partial melting. This application is similar to the use of Yb-in-clinopyroxene to estimate the degree of partial melting (Hao et al., 2012). For samples 07TB18 and 09TB128, their magma source (i.e., juvenile crust in the Gangdese belt) may have not undergone extreme metamorphism, and has thus likely the same chemical composition. The average zircon Hf content of sample 07TB18 (8883 ppm) is slightly higher than that of sample 09TB128 (8401 ppm), which reflects that the degree of partial melting of the former is lower. The measured water content (average and median) of sample 07TB18 is higher than that of sample 09TB128, which can be explained by the effect of partial melting. Assuming that the lower crust of the Indian plate (magma source of sample 07TB11) has similar Hf contents to the lower crust of the Gangdese belt, the higher average zircon Hf content of sample 07TB11 (than both samples 07TB18 and 09TB128) indicates that the degree of partial melting of sample 07TB11 is lower. However, the average zircon H_2O content of sample 07TB11 is lower than the latter two samples. Unlike other samples, sample 11SR02-1 was derived from the upper-middle crust. Hence, it is difficult to compare the degree of partial melting of sample 11SR02-1 with the samples derived from the lower crust. Based on the Hf and H_2O contents of the analyzed zircons, the differences in the degree of partial melting cannot account for the water difference for each sample.

5.1.5 *Charge balance*

Zircon contains many trace elements and tetravalent cations

(U, Th, and Hf), which are incorporated by the substitution of Zr to maintain charge balance. However, the substitution mechanism of trivalent REEs into zircon remains controversial. The pervasive mechanism (so-called "xenotime substitution") involves the coupling of trivalent REE or Y cations with pentavalent P cation to substitute the same amount of tetravalent Zr and Si cations (Finch et al., 2001). In fact, only a few analyzed results exhibit (REE+Y)/P atomic ratio that equals to unity (Hanchar et al., 2001; De Hoog et al., 2014; Yang W et al., 2016; Zhu et al., 2020), and hence charge excess exists in the zircon lattice if the "xenotime substitution" mechanism is the only way for the REE+Y and P incorporation. De Hoog et al. (2014) analyzed the crystalline zircon grains from the Mid-Atlantic Ridge gabbro. The zircon grains have higher (REE+Y)/P than unity, but the (REE+Y)/(H+P) atomic ratios≈1. These authors interpreted the H-incorporation mechanism as an excess REE+Y charge-balanced one. For the zircons with excess (REE+Y) to P, the H_2O can maintain the charge balance by coupling of H and excess (REE+Y) to replace Zr. Nevertheless, the (REE+Y)/(H+P) ratios of our zircon samples are wide-ranged and not equal or close to 1 (Figure 6). This indicates that the H-incorporation mechanism proposed by De Hoog et al. (2014) is not suitable for our case. Cui (2020) yielded similarly non-unity (REE+Y)/(H+P) ratios by performing FTIR, SIMS and LA-ICPMS analyses on a suite of zircon standards, and proposed multiple coupling mechanisms involving a range of coexisting elements (e.g., Al, Li, Mg) in zircons.

5.2 Controlling factors of magma water content

Considering that none of radiation damage, *T*-*P*-fO_2, magma evolution, melt fraction and charge balance can fully account for the H_2O-in-zircon change, we considered that the H_2O-in-zircon change can reflect the difference in magma water content.

5.2.1 Mode of melting (dehydration vs. water-fluxed)

Dehydration melting commonly involves the breakdown of hydrous minerals at a specific temperature and pressure, and under the condition that external fluid is absent. Water-fluxed melting involves the addition of free H_2O phase to facilitate partial melting. Although many authors argued against the possibility of large-scale water-fluxed melting in the crust, owing to the limited capacity for water accommodation in the crust (Yardley and Valley, 1997), some recent studies suggested universal occurrence of water-fluxed melting (Weinberg and Hasalová, 2015). The lower crust above the subduction zones is generally characterized by high electrical conductivity, reflecting the fluids released from the subducting slab (Li et al., 2003; Bai et al., 2010; Worzewski et al., 2010; Evans et al., 2014). By definition, water of dehydration melting is only derived from the breakdown of hydrous minerals, and hence the melt is water-unsaturated. In contrast, water-fluxed melting can produce water undersaturated or saturated magma, depending on the volume of fluid influx (Weinberg and Hasalová, 2015). The whole-rock K/Na ratio formed by dehydration melting is higher than that formed by water-fluxed melting (Douce and McCarthy, 1998). Moreover, the magmas produced by muscovite-dehydration have much higher Rb/Sr ratio and lower Sr-Ba contents (Inger and Harris, 1993). Different compositional trends of dehydration melting vs. water-fluxed melting were distinguished based on the Rb-Sr-Ba contents (Figure 8). In the Sr vs. Rb/Sr and Ba vs. Rb/Sr plots, the muscovite-dehydration melting trend is present for the Late Devonian Zhengga two-mica granite (Ma et al., 2019), whereas the water-fluxed melting trend is present for the Luomu diorite (~75 Ma), Lamda granodiorite (~48 Ma), and Chongmuda monzonite (~30 Ma) (Jiang et al., 2014) (Figure 8). Consequently, we proposed that the H_2O-in-zircon variation can record the different magma water contents

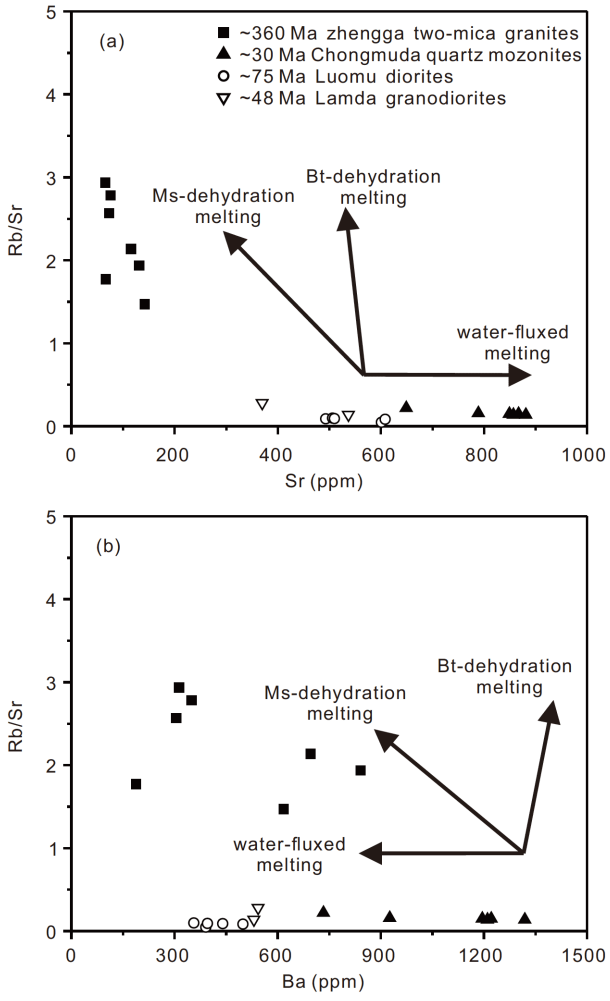

Figure 8 Diagrams of (a) Sr vs. Rb/Sr; (b) Ba vs. Rb/Sr. Whole-rock Rb-Sr-Ba data are from Jiang et al. (2014) and Ma et al. (2019). Melting trends are from Inger and Harris (1993).

caused by different modes of melting, with the magmas formed by muscovite dehydration melting being "drier" than those formed by water-fluxed melting.

5.2.2 Water content in crustal source and volume of water influx

Apart from the mode of melting, the water-content heterogeneity in the crust and the volume of water influx can also influence the magma water content. Geophysical studies found that the Phanerozoic lower crust has generally higher conductivity than that of the Precambrian cratonic crust (Hyndman and Shearer, 1989). Such conductivity difference likely reflects the H_2O content in the lower crust, with higher conductivity representing higher H_2O content (Hyndman and Shearer, 1989; Yang et al., 2006). Due to the incompatibility of water in magmas, the ancient crust that has experienced multiple episodes of dehydration processes (including metamorphism and partial melting) would retain lower amount of water. This inference is supported by the fact that the juvenile lithospheric mantle has higher H_2O content than the ancient lithospheric mantle, as supported by the H_2O content in NAMs from the mantle peridotites (Hao et al., 2012; Xu et al., 2019). The gabbros and hornblendites emplaced in the Late Cretaceous southern Tibet contain 20–70 vol.% hornblende, which can represent the water content of the juvenile Gangdese crust (Ma et al., 2013a, 2013b). Comparatively, the High Himalayan granulites (representing the lower crust of the Indian plate) contain <20 vol.% biotite and amphibole (Zhang L et al., 2018). This suggests that the ancient lower crust of the Indian plate contains lower water content than the juvenile crust of the Gangdese belt. Sample 09TB128 is likely sourced from the juvenile crust in the Lhasa block (in a continental subduction setting), where the water required for water-fluxed melting was likely released from the hydrous mineral decomposition in the lower crust. Sample 07TB11 (sourced from the ancient crust of the Indian plate) was also likely formed in a continental subduction setting, where the water required for water-fluxed melting was released from the ancient crust. Zircon water content of sample 09TB128 is higher than that of sample 07TB11. Considering the different hydrous mineral contents between the crustal sources that formed samples 09TB128 and 07TB11, we interpreted that the H_2O-in-zircon difference between these two samples reflects the more hydrated nature in the Gangdese lower crust than in the Indian plate. Sample 07TB18 (sourced from the juvenile crust in the Gangdese belt) was formed in an oceanic subduction setting, and the water required for the water-fluxed melting may have come mainly from the subducting oceanic crust and minor from the crustal input in the overlying Gangdese lower crust. The water influx for the formation of sample 07TB18 may have been much higher than that for the formation of sample 07TB11, as supported by the H_2O-in-zircon relation of 07TB18>07TB11.

6. Conclusions

SIMS analyses indicate that the average H_2O-in-zircon contents in both the Late Devonian two-mica granite and Oligocene quartz monzonite (251 ppm) are lower than those of the partial melting products of the juvenile crust, i.e., the diorite (448 ppm) and granodiorite (416 ppm) samples. Zircon $\delta^{18}O$ values and trace element compositions indicate that the difference in H_2O-in-zircon contents may not have caused by zircon radiation damage, or by the variation in temperature-pressure-fO_2 conditions, or by the degree of partial melting and magma fractionation. Instead, the H_2O-in-zircon heterogeneity likely reflects the difference in magma water contents. Integrated with published geophysical and geochemical studies, we suggested that the water contents of crust-derived magma generated in southern Tibet are controlled by the mode of melting, the water content of the crustal magma source and the free-H_2O influx. Facilitated by intraplate-extension related heating and decompression, dehydration melting of the crustal rocks may have occurred in the Late Devonian, whose resulting magmas were "drier" than those formed by the late Mesozoic-Cenozoic water-fluxed melting in the lower crust. In addition, melting products of the juvenile crust with voluminous hydrous minerals may have had much higher magma water content than those of the melting products of the ancient crust with small volume of hydrous minerals.

Acknowledgements *We thank three anonymous reviewers for their constructive comments that improved the manuscript substantially. We appreciate the help from Yanqing ZHANG for sample preparation. This work was supported by the National Natural Science Foundation of China (Grant No. 41673010) and the Second Tibetan Plateau Scientific Expedition and Research (STEP) (Grant No. 2019QZKK0702).*

References

Bai D, Unsworth M J, Meju M A, Ma X, Teng J, Kong X, Sun Y, Sun J, Wang L, Jiang C, Zhao C, Xiao P, Liu M. 2010. Crustal deformation of the eastern Tibetan plateau revealed by magnetotelluric imaging. Nat Geosci, 3: 358–362

Bau M. 1996. Controls on the fractionation of isovalent trace elements in magmatic and aqueous systems: Evidence from Y/Ho, Zr/Hf, and lanthanide tetrad effect. Contrib Mineral Petrol, 123: 323–333

Bell D R, Rossman G R. 1992. Water in Earth's mantle: The role of nominally anhydrous minerals. Science, 255: 1391–1397

Belousova E A, Griffin W L, O'Reilly S, Fisher N I. 2002. Igneous zircon: Trace element composition as an indicator of source rock type. Contrib Mineral Petrol, 143: 602–622

Breiter K, Lamarão C N, Borges R M K, Dall'Agnol R. 2014. Chemical characteristics of zircon from A-type granites and comparison to zircon of S-type granites. Lithos, 192-195: 208–225

Burnham A D, Berry A J. 2012. An experimental study of trace element partitioning between zircon and melt as a function of oxygen fugacity. Geochim Cosmochim Acta, 95: 196–212

Chakoumakos B C, Murakami T, Lumpkin G R, Ewing R C. 1987. Alpha-decay-induced fracturing in zircon: The transition from the crystalline to the metamict state. Science, 236: 1556–1559

Chapman J B, Ducea M N, DeCelles P G, Profeta L. 2015. Tracking

changes in crustal thickness during orogenic evolution with Sr/Y: An example from the North American Cordillera. Geology, 43: 919–922
Cherniak D J, Watson E B. 2001. Pb diffusion in zircon. Chem Geol, 172: 5–24
Collins W J, Beams S D, White A J R, Chappell B W. 1982. Nature and origin of A-type granites with particular reference to southeastern Australia. Contrib Mineral Petrol, 80: 189–200
Corfu F, Hanchar J M, Hoskin P W O, Kinny P. 2003. Atlas of zircon textures. Rev Mineral Geochem, 53: 469–495
Cui Z X. 2020. Measurement, incorporation mechanism and geological application of H2O-in-zircon (in Chinese with English abstract). Master Dissertation. Guangzhou: Guangzhou Institute of Geochemistry, Chinese Academy of Sciences. 1–119
De Hoog J C M, Lissenberg C J, Brooker R A, Hinton R, Trail D, Hellebrand E. 2014. Hydrogen incorporation and charge balance in natural zircon. Geochim Cosmochim Acta, 141: 472–486
Demouchy S, Bolfan-Casanova N. 2016. Distribution and transport of hydrogen in the lithospheric mantle: A review. Lithos, 240-243: 402–425
Dong X, Zhang Z, Liu F, He Z, Lin Y. 2014. Late Paleozoic intrusive rocks from the southeastern Lhasa terrane, Tibetan Plateau, and their Late Mesozoic metamorphism and tectonic implications. Lithos, 198-199: 249–262
Douce A E P, McCarthy T C. 1998. Melting of crustal rocks during continental collision and subduction. In: Hacker B R, Liou J G, eds. When Continents Collide: Geodynamics and Geochemistry of Ultrahigh-Pressure Rocks. Dordrecht: Springer. 27–55
Evans R L, Wannamaker P E, McGary R S, Elsenbeck J. 2014. Electrical structure of the central Cascadia subduction zone: The EMSLAB Lincoln Line revisited. Earth Planet Sci Lett, 402: 265–274
Ferry J M, Watson E B. 2007. New thermodynamic models and revised calibrations for the Ti-in-zircon and Zr-in-rutile thermometers. Contrib Mineral Petrol, 154: 429–437
Finch R J, Hanchar J M, Hoskin P W O, Burns P C. 2001. Rare-earth elements in synthetic zircon: Part 2. A single-crystal X-ray study of xenotime substitution. Am Miner, 86: 681–689
Geisler T, Pidgeon R T, van Bronswijk W, Kurtz R. 2002. Transport of uranium, thorium, and lead in metamict zircon under low-temperature hydrothermal conditions. Chem Geol, 191: 141–154
Hanchar J M, Finch R J, Hoskin P W O, Watson E B, Cherniak D J, Mariano A N. 2001. Rare earth elements in synthetic zircon: Part 1. Synthesis, and rare earth element and phosphorus doping. Am Miner, 86: 667–680
Hao Y, Xia Q, Liu S, Feng M, Zhang Y. 2012. Recognizing juvenile and relict lithospheric mantle beneath the North China Craton: Combined analysis of H_2O, major and trace elements and Sr-Nd isotope compositions of clinopyroxenes. Lithos, 149: 136–145
Hauri E H, Gaetani G A, Green T H. 2006. Partitioning of water during melting of the Earth's upper mantle at H_2O-undersaturated conditions. Earth Planet Sci Lett, 248: 715–734
Hoskin P W O, Schaltegger U. 2003. The composition of zircon and igneous and metamorphic petrogenesis. Rev Mineral Geochem, 53: 27–62
Hu B Q, Wang F Z, Sun Z X, Liu C D, Bai L H. 2003. The pressure gradient in the lithosphere (in Chinese with English abstract). Earth Sci Front, 10: 129–133
Hyndman R D, Shearer P M. 1989. Water in the lower continental crust: Modelling magnetotelluric and seismic reflection results. Geophys J Int, 98: 343–365
Inger S, Harris N. 1993. Geochemical constraints on leucogranite magmatism in the Langtang Valley, Nepal Himalaya. J Petrol, 34: 345–368
Ji W Q, Wu F Y, Chung S L, Li J X, Liu C Z. 2009. Zircon U-Pb geochronology and Hf isotopic constraints on petrogenesis of the Gangdese batholith, southern Tibet. Chem Geol, 262: 229–245
Ji W Q, Wu F Y, Chung S L, Liu C Z. 2012. Identification of Early Carboniferous granitoids from Southern Tibet and implications for terrane assembly related to the paleo-tethyan evolution. J Geol, 120: 531–541
Jiang Z Q, Wang Q, Wyman D A, Tang G J, Jia X H, Yang Y H, Yu H X. 2011. Origin of ~30 Ma Chongmuda adakitic intrusive rocks in the southern Gangdese region, southern Tibet: Partial melting of the northward subducted Indian continent crust (in Chinese with English abstract)? Geochimica, 40: 126–146
Jiang Z Q, Wang Q, Wyman D A, Li Z X, Yang J H, Shi X B, Ma L, Tang G J, Gou G N, Jia X H, Guo H F. 2014. Transition from oceanic to continental lithosphere subduction in southern Tibet: Evidence from the Late Cretaceous-Early Oligocene (~91–30 Ma) intrusive rocks in the Chanang-Zedong area, southern Gangdese. Lithos, 196-197: 213–231
Johnson E A. 2006. Water in nominally anhydrous crustal minerals: Speciation, concentration, and geologic significance. Rev Mineral Geochem, 62: 117–154
Karato S. 1990. The role of hydrogen in the electrical conductivity of the upper mantle. Nature, 347: 272–273
Li S, Unsworth M J, Booker J R, Wei W, Tan H, Jones A G. 2003. Partial melt or aqueous fluid in the mid-crust of Southern Tibet? Constraints from INDEPTH magnetotelluric data. Geophys J Int, 153: 289–304
Li X H, Long W G, Li Q L, Liu Y, Zheng Y F, Yang Y H, Chamberlain K R, Wan D F, Guo C H, Wang X C, Tao H. 2010. Penglai zircon megacrysts: A potential new working reference material for microbeam determination of Hf-O isotopes and U-Pb age. Geostand Geoanal Res, 34: 117–134
Luo Y, Ayers J C. 2009. Experimental measurements of zircon/melt trace-element partition coefficients. Geochim Cosmochim Acta, 73: 3656–3679
Ma L, Kerr A C, Wang Q, Jiang Z Q, Tang G J, Yang J H, Xia X P, Hu W L, Yang Z Y, Sun P. 2019. Nature and evolution of crust in Southern Lhasa, Tibet: Transformation from microcontinent to juvenile terrane. J Geophys Res Solid Earth, 124: 6452–6474
Ma L, Wang Q, Li Z X, Wyman D A, Jiang Z Q, Yang J H, Gou G N, Guo H F. 2013a. Early Late Cretaceous (ca. 93 Ma) norites and hornblendites in the Milin area, eastern Gangdese: Lithosphere-asthenosphere interaction during slab roll-back and an insight into early Late Cretaceous (ca. 100–80 Ma) magmatic "flare-up" in southern Lhasa (Tibet). Lithos, 172–173: 17–30
Ma L, Wang Q, Wyman D A, Jiang Z Q, Yang J H, Li Q L, Gou G N, Guo H F. 2013b. Late Cretaceous crustal growth in the Gangdese area, southern Tibet: Petrological and Sr-Nd-Hf-O isotopic evidence from Zhengga diorite-gabbro. Chem Geol, 349-350: 54–70
Manning C E. 2018. Fluids of the lower crust: Deep is different. Annu Rev Earth Planet Sci, 46: 67–97
Murakami T, Chakoumakos B C, Ewing R C, Lumpkin G R, Weber W J. 1991. Alpha-decay event damage in zircon. Am Miner, 76: 9–10, 1510–1532
Németh B, Török K, Kovács I, Szabó C, Abart R, Dégi J, Mihály J, Németh C. 2015. Melting, fluid migration and fluid-rock interactions in the lower crust beneath the Bakony-Balaton Highland volcanic field: A silicate melt and fluid inclusion study. Miner Petrol, 109: 217–234
Pidgeon R T, Nemchin A A, Cliff J. 2013. Interaction of weathering solutions with oxygen and U-Pb isotopic systems of radiation-damaged zircon from an Archean granite, Darling Range Batholith, Western Australia. Contrib Mineral Petrol, 166: 511–523
Pidgeon R T, Nemchin A A, Roberts M P, Whitehouse M J, Bellucci J J. 2019. The accumulation of non-formula elements in zircons during weathering: Ancient zircons from the Jack Hills, Western Australia. Chem Geol, 530: 119310
Pidgeon R T, Nemchin A A, Whitehouse M J. 2017. The effect of weathering on U-Th-Pb and oxygen isotope systems of ancient zircons from the Jack Hills, Western Australia. Geochim Cosmochim Acta, 197: 142–166
Rubatto D, Hermann J. 2007. Experimental zircon/melt and zircon/garnet trace element partitioning and implications for the geochronology of crustal rocks. Chem Geol, 241: 38–61
Schmädicke E, Gose J, Reinhardt J, Will T M, Stalder R. 2015. Garnet in cratonic and non-cratonic mantle and lower crustal xenoliths from southern Africa: Composition, water incorporation and geodynamic

constraints. Precambrian Res, 270: 285–299
Seaman S J, Williams M L, Jercinovic M J, Koteas G C, Brown L B. 2013. Water in nominally anhydrous minerals: Implications for partial melting and strain localization in the lower crust. Geology, 41: 1051–1054
Sun G, Li X P, Duan W, Chen S, Wang Z, Zhao L, Feng Q. 2018. Metamorphic characteristics and tectonic implications of the Kadui Blueschist in the Central Yarlung Zangbo Suture Zone, Southern Tibet. J Earth Sci, 29: 1026–1039
Sun S, McDonough W F. 1989. Chemical and isotopic systematics of oceanic basalts: Implications for mantle composition and processes. Geol Soc Lond Spec Publ, 42: 313–345
Trail D, Boehnke P, Savage P S, Liu M C, Miller M L, Bindeman I. 2018. Origin and significance of Si and O isotope heterogeneities in Phanerozoic, Archean, and Hadean zircon. Proc Natl Acad Sci USA, 115: 10287–10292
Trail D, Mojzsis S J, Harrison T M, Schmitt A K, Watson E B, Young E D. 2007. Constraints on Hadean zircon protoliths from oxygen isotopes, Ti-thermometry, and rare earth elements. Geochem Geophys Geosyst, 8: Q06014
Ushikubo T, Kita N T, Cavosie A J, Wilde S A, Rudnick R L, Valley J W. 2008. Lithium in Jack Hills zircons: Evidence for extensive weathering of Earth's earliest crust. Earth Planet Sci Lett, 272: 666–676
Valley J W. 2003. Oxygen isotopes in Zircon. Rev Mineral Geochem, 53: 343–385
Wang X L, Coble M A, Valley J W, Shu X J, Kitajima K, Spicuzza M J, Sun T. 2014. Influence of radiation damage on Late Jurassic zircon from southern China: Evidence from *in situ* measurements of oxygen isotopes, laser Raman, U-Pb ages, and trace elements. Chem Geol, 389: 122–136
Watenphul A, Wunder B, Wirth R, Heinrich W. 2010. Ammonium-bearing clinopyroxene: A potential nitrogen reservoir in the Earth's mantle. Chem Geol, 270: 240–248
Weinberg R F, Hasalová P. 2015. Water-fluxed melting of the continental crust: A review. Lithos, 212-215: 158–188
Whalen J B, Currie K L, Chappell B W. 1987. A-type granites: Geochemical characteristics, discrimination and petrogenesis. Contrib Mineral Petrol, 95: 407–419
Woodhead J A, Rossman G R, Silver L. 1991. The metamictization of zircon: Radiation dose-dependent structural characteristics. Am Miner, 76: 1–2
Worzewski T, Jegen M, Kopp H, Brasse H, Taylor Castillo W. 2010. Magnetotelluric image of the fluid cycle in the Costa Rican subduction zone. Nat Geosci, 4: 108–111
Wu F Y, Liu X C, Ji W Q, Wang J M, Yang L. 2017. Highly fractionated granites: Recognition and research. Sci China Earth Sci, 60: 1201–1219
Xia X P, Cui Z X, Li W, Zhang W F, Yang Q, Hui H, Lai C K. 2019. Zircon water content: Reference material development and simultaneous measurement of oxygen isotopes by SIMS. J Anal At Spectrom, 34: 1088–1097
Xia X, Sun M, Zhao G, Wu F, Xu P, Zhang J, Luo Y. 2006. U-Pb and Hf isotopic study of detrital zircons from the Wulashan khondalites: Constraints on the evolution of the Ordos Terrane, Western Block of the North China Craton. Earth Planet Sci Lett, 241: 581–593
Xu Q, Liu J, He H, Zhang Y. 2019. Nature and evolution of the lithospheric mantle revealed by water contents and He-Ar isotopes of peridotite xenoliths from Changbaishan and Longgang basalts in Northeast China. Sci Bull, 64: 1325–1335
Yang G C, Yang X Z, Hao Y T, Xia Q K. 2012a. Water content difference between continental lower crust and lithospheric mantle: granulite and peridotite xenoliths hosted in basalts from Junan, Shandong Province (in Chinese with English abstract). Acta Petrol Mineral, 31: 691–700
Yang G C, Yang X Z, Xia Q K. 2012b. Temporal variation of water content in the lower continental crust: Evidence from feldspar in mafic granulites (in Chinese with English abstract). Acta Petrol Mineral, 31: 565–577
Yang W, Lin Y, Hao J, Zhang J, Hu S, Ni H. 2016. Phosphorus-controlled trace element distribution in zircon revealed by NanoSIMS. Contrib Mineral Petrol, 171: 28
Yang X Z, Xia Q K, Yu H M, Hao Y T. 2006. The possible effect of hydrogen on the high electrical conductivity in the lower continental crust (in Chinese with English abstract). Adv Earth Sci, 21: 31–38
Yang X Z, Deloule E, Xia Q K, Fan Q C, Feng M. 2008. Water contrast between Precambrian and Phanerozoic continental lower crust in eastern China. J Geophys Res, 113: B08207
Yang X, Keppler H, Li Y. 2016. Molecular hydrogen in mantle minerals. Geochem Persp Lett, 2: 160–168
Yardley B W D, Valley J W. 1997. The petrologic case for a dry lower crust. J Geophys Res, 102: 12173–12185
Yin A, Harrison T M. 2000. Geologic evolution of the Himalayan-Tibetan Orogen. Annu Rev Earth Planet Sci, 28: 211–280
Zhang L, Ren Z Y, Xia X P, Yang Q, Hong L B, Wu D. 2019. *In situ* determination of trace elements in melt inclusions using laser ablation inductively coupled plasma sector field mass spectrometry. Rapid Commun Mass Spectrom, 33: 361–370
Zhang L, Ye Y, Qin S, Jin Z. 2018. Water in the thickened lower crust of the Eastern Himalayan Orogen. J Earth Sci, 29: 1040–1048
Zhang P P. 2015. Hydrogen diffusion in NAMs: Andradite garnet and zircon. Doctoral Dissertation. Hefei: University of Science and Technology of China
Zhang W, Xia X, Zhang Y, Peng T, Yang Q. 2018. A novel sample preparation method for ultra-high vacuum (UHV) secondary ion mass spectrometry (SIMS) analysis. J Anal At Spectrom, 33: 1559–1563
Zhu D C, Zhao Z D, Niu Y, Dilek Y, Hou Z Q, Mo X X. 2013. The origin and pre-Cenozoic evolution of the Tibetan Plateau. Gondwana Res, 23: 1429–1454
Zhu Z, Campbell I H, Allen C M, Burnham A D. 2020. S-type granites: Their origin and distribution through time as determined from detrital zircons. Earth Planet Sci Lett, 536: 116140

(Responsible editor: Yongfei ZHENG)